Enhancing Transport Barriers with Swimming Microorganisms in Chaotic Flows: *Supplementary Materials*

Ranjiangshang Ran[1,2] and Paulo E. Arratia[1,*]

[1] *Department of Mechanical Engineering and Applied Mechanics, University of Pennsylvania, Philadelphia, PA 19104, USA*

[2] *Department of Physics, Emory University, Atlanta, GA 30322, USA*

1 Experimental Setup

Figure S1 shows the flow cell experimental setup, which consists of a 10 cm × 10 cm flow chamber, two graphite electrodes, a thin layer of electrolytic solution (2% wt. KCl and 1% wt. NaCl aqueous solution) and an array of permanent magnets beneath it. The polarities and positions of the magnets are generated by a random number generator, with an average spacing of $L = 6$ mm. Each magnet has a diameter of 4.8 mm, and a magnetic flux density 0.66 T. We impose a sinusoidal alternating current (AC) of 1.2 A and 0.2 Hz through graphite electrodes. The induced Lorentz force of conducting ions in the solution creates spatially disordered vortices.

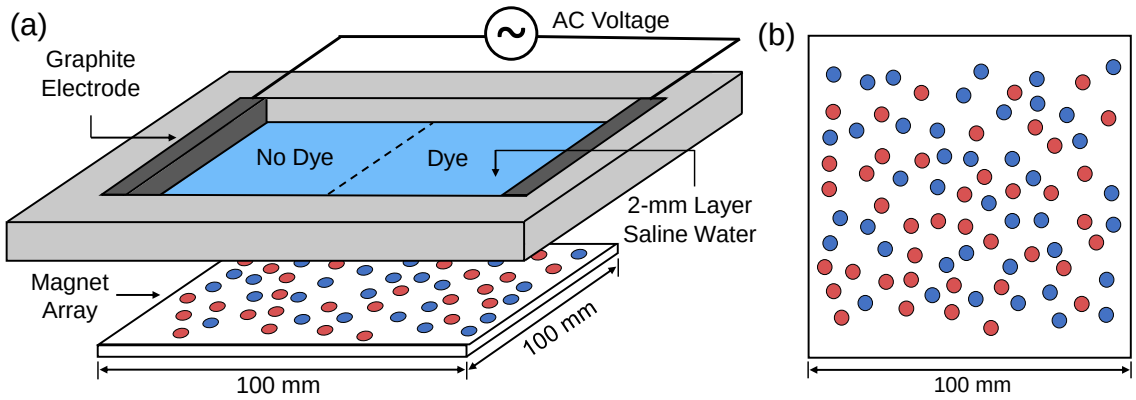

Fig. S1. (a) Schematic of the experimental setup of the flow cell apparatus. A thin layer of buffer solution or active suspension is placed above an array of magnets of alternating polarity. A sinusoidal voltage imposed by the electrodes induces Lorentz force in the fluid layer and drive the mixing. In dye mixing experiments, the right half of the fluid layer is labeled with a fluorescent dye. (b) Schematic of the spatially disordered magnet array. The position of the magnets are generated by random number generator. The colors of blue and red represent the north and south poles, respectively.

2 Characterization of Velocity Fields

Figure S2 shows the velocity and vorticity fields of the magnetically controlled flow. Both fields are measured at the first peak ($t = T/4$) of the time-periodic flow, where $T = 5$ s in the flow period. We

* Corresponding author: parratia@seas.upenn.edu.

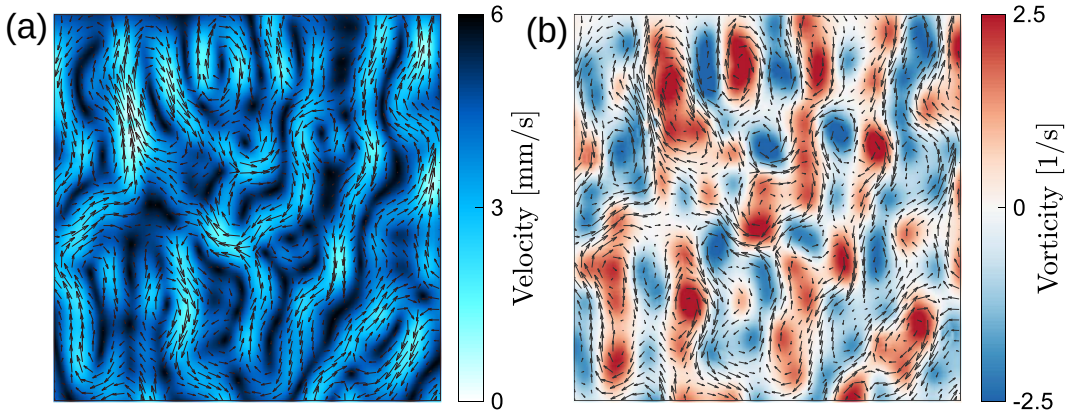

Fig. S2. Velocity and vorticity fields measured from particle tracking velocimetry (PTV), for experiments at Reynolds number $Re = 7.2$ and path length $p = 1.0$. Both fields are measured at the first peak of the time-periodic flow, $t = T/4$, where $T = 5$ s is the flow period. The arrows are velocity vectors and the color codes are (a) the magnitude of the velocity field $|\mathbf{v}|$, and (b) the vorticity field, defined as the curl of velocity field $\boldsymbol{\omega} = \nabla \times \mathbf{v}$. Plotted here is the out-of-plane component of the vorticity field, ω_z.

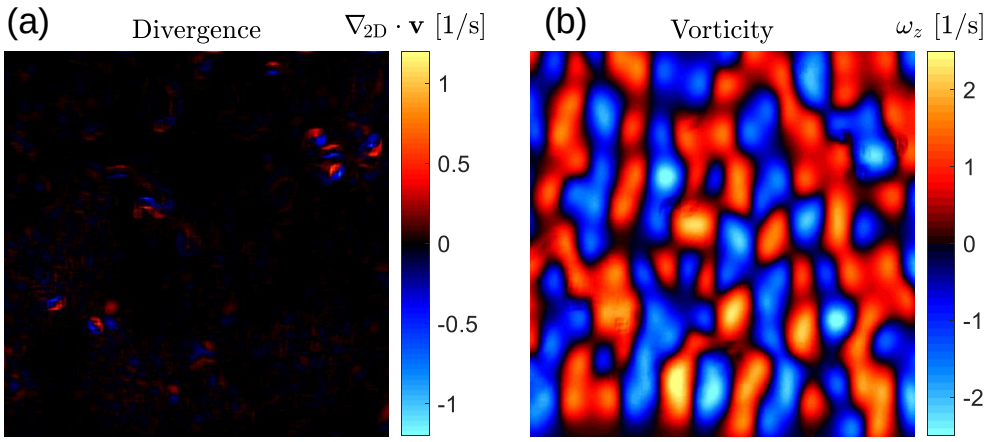

Fig. S3. (a) The two-dimensional divergence of velocity field, $\nabla_{2D} \cdot \mathbf{v} = \partial u/\partial x + \partial v/\partial y$. (b) The out-of-plane component of the vorticity field, $\omega_z = \partial v/\partial x - \partial u/\partial y$. Both fields are measured at the first peak of the a sinusoidal flow period ($t = T/4$).

characterize how two-dimensional (2D) our flow is by computing 2D divergence of the velocity field, $\nabla_{2D} \cdot \mathbf{v} = \partial u/\partial x + \partial v/\partial y$, where u and v are velocity components in the x- and y-direction, respectively. Due to incompressibility, we know that $\nabla_{2D} \cdot \mathbf{v} = -\partial w/\partial z$, where w denotes the three-dimensional velocity components in the z-direction. As a control, we also calculate the out-of-plane vorticity (ω_z) that is defined as: $\omega_z = \partial v/\partial x - \partial u/\partial y$. Figure S3 plots $\nabla_{2D} \cdot \mathbf{v}$ and ω_z in the same color code for comparison. We notice that the 2D divergence is nearly zero everywhere except in certain small regions due to the measurement noise. **This suggests that our flow is essentially two-dimensional.**

To further quantify the two-dimensionality, we calculate the root-mean-square (RMS) divergence and vorticity, averaged for the whole flow field. Figure S4 plots the field-averaged RMS divergence, $\langle|\nabla_{2D} \cdot \mathbf{v}|^2\rangle^{1/2}$, and RMS vorticity, $\langle\omega_z^2\rangle^{1/2}$, as a function of time in one flow period, for both the buffer and the active suspension. We find that the RMS divergence is approximately at $\mathcal{O}(10^{-2})$ of the RMS vorticity, for both the buffer and the active cases. While this indicates good accuracy, small regions of non-zero divergence (Fig. S3) may still cause passive particles to accumulate in the flow fields, especially for particle trajectories integrated for longer times (> 50 periods). This small departure from an ideal two-dimensional (divergence-free) velocity field likely causes the unwanted accumulation of passive particles observed in the simulations.

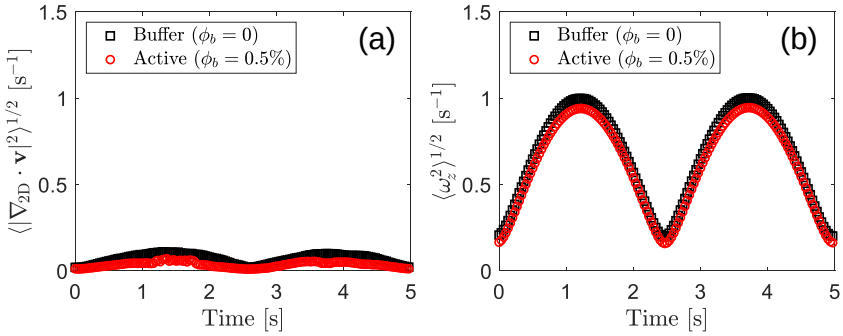

Fig. S4. (a) The RMS divergence $\langle|\nabla_{2D} \cdot \mathbf{v}|^2\rangle^{1/2}$ as a function of time for both the buffer and active cases. (b) the RMS vorticity $\langle\omega_z^2\rangle^{1/2}$ as a function of time for both the buffer and active cases.

3 Alignment of Active Particles

The alignment of the symmetric axis of the active particles, $\mathbf{q}$, with tangent of the elliptic LCSs, $\mathbf{t}$, is examined by their inner product $\mathbf{q} \cdot \mathbf{t}$, in Figure 4(b). We find a slight bias towards the positive peak, $\mathbf{q} \cdot \mathbf{t} = +1$, for active particles, and such bias is absent for passive particles. This suggests active particles are more likely to align parallel to the tangent of elliptic LCSs (i.e., they prefer to swim in the direction of the vortex circulation). We now further characterize this bias in the alignment by calculating the statistical mean of the inner product, $\langle \mathbf{q} \cdot \mathbf{t} \rangle$. Figure S5(a) shows $\langle \mathbf{q} \cdot \mathbf{t} \rangle$ for both the passive and active particles. We find that $\langle \mathbf{q} \cdot \mathbf{t} \rangle > 0$ is true for active particles, while $\langle \mathbf{q} \cdot \mathbf{t} \rangle \approx 0$ at all times for passive particles. The suggests active particles prefer to swim in the direction of the vortex circulation, while (non swimming) passive particles do not have a preference in parallel/anti-parallel alignment.

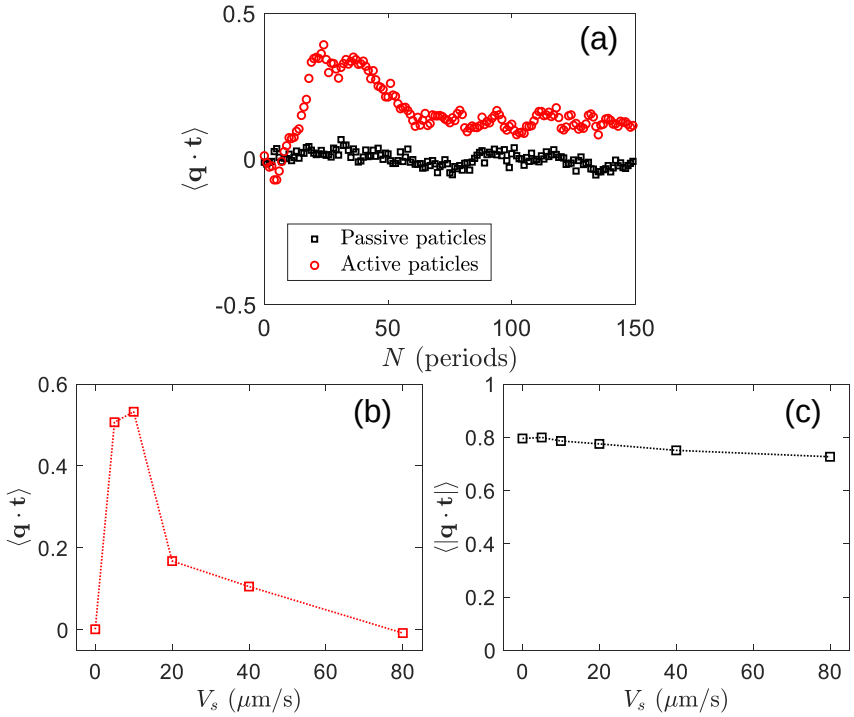

Fig. S5. (a) The inner product between particle orientation vector, $\mathbf{q}$, and the tangent vector of the elliptic LCSs, $\mathbf{t}$, as a function of time for passive and active particles. (b) The ensemble average of the inner product, $\langle \mathbf{q} \cdot \mathbf{t} \rangle$, as a function of swimming speed, V_s. (c) The ensemble average of the absolute value of the inner product, $\langle |\mathbf{q} \cdot \mathbf{t}| \rangle$, as a function of V_s.

We also investigate the bias in parallel/anti-parallel alignment for active particles of different swimming speeds (V_s = 0, 5, 10, 20, 40, and 80 μm/s). Figure S5(b) plots $\langle \mathbf{q} \cdot \mathbf{t} \rangle$ as a function of swimming speeds. We find that active particles of lower swimming speed are more biased to align parallel to the tangent and $\langle \mathbf{q} \cdot \mathbf{t} \rangle > 0$, while active particles of higher swimming speed do not seem to have a preference between parallel and anti-parallel alignment and $\langle \mathbf{q} \cdot \mathbf{t} \rangle \approx 0$. Figure S5(c) characterizes the overall alignment (i.e., align *vs.* not align) by calculating $\langle |\mathbf{q} \cdot \mathbf{t}| \rangle$ for different swimming speeds. We find that the overall alignment of active particles is quite similar for all swimming speeds. These results [Figures S5(b) and S5(c)] suggest that the swimming speed does not seem to affect the overall alignment of active particles, but does affect their preferred direction of alignment (parallel or anti-parallel).

4 Possibility of Ekman transport

Since the Lorentz force follows a similar equation as the Coriolis force, it is plausible Ekman transport may exist in our system. However, below we will demonstrate that Ekman pumping is not present in our flow system; or, if present, the effect is minimal. We begin by defining an Ekman number for the Lorentz force. The classic Ekman number is the ratio between viscous force and Coriolis force, which is defined as:

$$Ek = \frac{\nu}{2\Omega H^2}, \tag{1}$$

where ν is the fluid kinematic viscosity, Ω is the angular velocity of the rotation of the reference frame, and H is the characteristic depth of the flow system. Here, the force density of the Lorentz force is: $d\,\mathbf{F}_B/d\,V = \rho_q\,(\mathbf{v} \times \mathbf{B})$, compared to the force density of the Coriolis force: $d\,\mathbf{F}_\Omega/d\,V = 2\rho\,(\mathbf{v} \times \mathbf{\Omega})$, where $\mathbf{v}$ is fluid velocity, $\mathbf{B}$ is the strength of the magnetic field, and ρ_q and ρ are the charge density and mass density of the fluid, respectively. By comparison, the corresponding Ekman number for the Lorentz force is:

$$Ek_B = \frac{\nu}{(B\rho_q/\rho)\,H^2}. \tag{2}$$

For our buffer solution of 2% wt. KCl and 1% wt. NaCl, the total ion (K^+, Na^+, Cl^-) concentration is 0.88 mol/L. Given that the charge of 1 mol of electrons is 96500 C, the charge density is $\rho_q = 8.5 \times 10^4$ C/L. The density of water is $\rho = 1$ kg/L. The magnetic flux density of our permanent magnets is $B = 0.66$ T = 0.66 kg/(C. s), and the thickness of our fluid layer is $H = 2$ mm. The kinematic viscosity of water is $\nu = 1$ mm^2/s. These result in a magnetic Ekman number of:

$$Ek_B = \frac{\nu}{(B\rho_q/\rho)\,H^2} = \frac{1\text{ mm}^2/\text{s} \times 1\text{ kg/L}}{0.66\text{ kg/(C.s)} \times 8.5 \times 10^4\text{ C/L} \times 4\text{ mm}^2} = 4.5 \times 10^{-6} \tag{3}$$

The thickness of the Ekman layer can be estimated at $Ek_B\,(d) \sim 1$, which yields that $d_B \sim \sqrt{\nu\rho/B\rho_q}$ for the Lorentz force. This estimates an Ekman layer thickness of:

$$d_B = \sqrt{\frac{\nu\rho}{B\rho_q}} = \sqrt{\frac{1\text{ mm}^2/\text{s} \times 1\text{ kg/L}}{0.66\text{ kg/(C.s)} \times 8.5 \times 10^4\text{ C/L}}} = 0.004\text{ mm}, \tag{4}$$

which is the thickness near the bottom no-slip boundary where the Ekman transport is significant. Compared to our fluid layer thickness of $H = 2$ mm, the Ekman layer thickness is negligible. This result indicates that the magnetic forcing is so strong that the flow profile is almost the same throughout the whole fluid layer outside the Ekman layer (0.004 mm $< d <$ 2 mm), despite the presence of a no-slip boundary. Furthermore, the bottom surface is treated with a hydrophobic PDMS coating (water contact angle $> 100^\circ$) to reduce friction. Thus, we believe that Ekman transport due to the Lorentz force is negligible in our system. As for the Ekman transport due to Coriolis effect, we notice that the Coriolis force and the Lorentz force can be combined into a single term in the momentum equation:

$$\frac{d\,(\mathbf{F}_B + \mathbf{F}_\Omega)}{d\,V} = \mathbf{v} \times (\rho_q \mathbf{B} + 2\rho\mathbf{\Omega})\,. \tag{5}$$

However, the strength of the Coriolis force is much weaker compared to the Lorentz force: $|\mathbf{F}_\Omega|/|\mathbf{F}_B| = 2\rho\Omega/\rho_q B = 2.8 \times 10^{-5}$, for a typical flow vorticity of $\omega = 2\Omega = 2$ s^{-1}. This means that the Coriolis force is too weak to modify the flow profile imposed by such a strong magnetic forcing. Therefore, we conclude that Ekman pumping is not present in our system.

5 Movie Captions

Movie 1. Stroboscopic video of dye mixing experiments, for mixing in the buffer solution (left) and a bacterial suspension of a volume fraction $\phi_b = 0.5\%$ (right).

Movie 2. Real time video of the dye field (left column) and the TRA field (right column), for mixing in the buffer solution (top row) and a bacterial suspension of a volume fraction $\phi_b = 0.5\%$ (bottom row).

Movie 3. Spatial distribution of passive particles (left) and active particles (right) in numerical simulations. The particles are colored by their normalized local number density ρ_N/ρ_0.

Movie 4. Stroboscopic trajectories of a passive particle (blue) and an active particle (orange) within Lagrangian vortices. The color map is the TRA field. The swimming direction of the active particle is illustrated by an arrow, while the (non-swimming) passive particle is represented as a bar.